RSC Advances

PAPER

View Article Online
View Journal | View Issue

Cite this: *RSC Adv.*, 2026, **16**, 18242

Effect of Bi^{3+} on the physical, mechanical, and dielectric properties of cadmium silicate glasses for energy storage devices

A. G. Darwish, *[a] Mohamed I. Farouk,[b] Mostafa I. Abdelglil[c] and H. A. Abo-Mosallam*[d]

Glasses with the composition of (60 − *X*)CdO–*X*Bi_2O_3–40SiO_2 (*X* = 0, 7.5, 15, and 30 mol%) were synthesized by melt-quenching. Their physical properties and FTIR spectra confirmed that the network strength weakened with the increase in CdO substitution by Bi_2O_3. The incorporation of Bi_2O_3 disrupts Si–O–Si bonds, forming non-bridging oxygen atoms that increase the molar volume and reduce the packing density. Dielectric spectra (0.1 Hz–10 MHz and 30–150 °C) showed increased permittivity and dielectric loss with Bi_2O_3 addition, strong frequency/temperature dependence, and thermally activated mid-frequency relaxations. The AC conductivity increased with the frequency: gradually (0.1–10 Hz), moderately (10 Hz–100 kHz), and sharply (1–10 MHz). The permittivity ranges are 18–27 (*X* = 0), 17–45 (*X* = 7.5), 17–55 (*X* = 15), and 24–65 (*X* = 30), with maxima at 0.1 Hz and over a temperature range of 30–150 °C. Doped samples exhibited conductivity shoulders coinciding with loss peaks. Mechanical moduli and microhardness decreased with Bi_2O_3 addition, confirming network softening. These glasses combined high dielectric performance and thermal stability, with potential for reprocessing, making them suitable for power-electronics components used in applications such as electric mobility, solar inverters, and wind-turbine converters.

Received 1st March 2026
Accepted 20th March 2026

DOI: 10.1039/d6ra01777k

rsc.li/rsc-advances

1 Introduction

Glass is currently the subject of extensive research because it is a promising material with a wide range of properties that qualify it for use in advanced applications in many fields. Recently, glass materials have been used in modern technological applications such as medical device fabrication, radiation protection, optics, and electronics.[1,2] Glass properties can be adjusted over a wide range through compositional design, enabling applications across many fields. They are also easy to prepare, environmentally friendly, inexpensive, and recyclable.[3,4] Oxide glasses, including sol–gel and melt-quenched varieties, dominate advanced material development.[5,6] Glasses are used in various modern electrical applications, such as in thermal sensors and energy storage capacitors, due to their tunable electrical properties, including dielectric constant, electrical conductivity, and dielectric loss.[7,8]

Glasses are mostly synthesized by a melt-quenching method. Oxide glasses are classified according to their network-forming oxides, with silicate, borate, and phosphate systems being the most widely studied. Silicon oxide (SiO_2) is a primary glass former that builds the main network structure, providing good chemical and thermal resistance.[9,10] Silicate-based glasses stand out among all vitreous materials due to their remarkable capacitive and energy-storage capabilities, particularly in capacitor applications.[11,12] Silicate glasses make good base materials because they are mechanically stable and transparent but have low permittivity. Adding CdO introduces heavy polarizable ions that raise permittivity, but the resulting network remains relatively rigid, which constrains dipolar relaxation. The addition of various elements to the glass network, such as transition-metal oxides (TMs) and heavy metals (HMOs), improves the properties and stability of the glass. Among the many appealing qualities of cadmium oxide (CdO) are its high molecular weight and density, strong polarizability and transparency, as well as high thermal stability. When CdO is added to glass networks, amorphous materials are created that can be used in a variety of applications, including in solar panels and batteries.[13,14] CdO functions as a network intermediate in these systems, contributing to electronic polarizability while also introducing non-bridging oxygens (NBOs) that enhance ionic polarizability and mobility. The electronic contribution improves the optical absorption and dielectric response, which are advantageous for photovoltaic applications, whereas NBO-facilitated ionic transport supports charge conduction in

[a]*Department of Microwave Physics and Dielectrics, Physics Research Institute, National Research Centre, 33 El-Buhouth St, Dokki, Cairo 12622, Egypt*
[b]*College of Engineering, Deanship of Scientific Research, Imam Mohammad Ibn Saud Islamic University (IMSIU), Riyadh 11432, Saudi Arabia*
[c]*Colleges of Medical Technical, Al-Farahidi University, Baghdad 00964, Iraq*
[d]*Glass Research Department, National Research Centre, 33 El-Buhouth St, Dokki, Cairo 12622, Egypt. E-mail: abomosallamnrc@gmail.com; ha.ebrahim@nrc.sci.eg*

energy storage systems. Additionally, Cd^{2+} incorporation can introduce localized defect states within the glass network, influencing conductivity without requiring band-like transport as in crystalline materials. Cadmium oxide (CdO) acts as an intermediate in the glass network; it may take part in the glass network's building formers (CdO_4 units) and/or act as a modifier of the glass structure (CdO_6 units). The role of CdO in the glass network depends on its concentration and the overall glass composition.[15,16] Furthermore, the presence of cadmium in the glass network enhances the physical, chemical, and optical properties of the synthesized glass.[15,16] Because of their many superior physical and optical qualities, glasses containing heavy metal oxides (HMOs) such as Bi_2O_3 are ideal for cutting-edge applications in devices like fiber optics, fiber lasers, oscillators, and amplifiers.[17,18] Additionally, bismuth silicate glasses are becoming more and more popular in a variety of optical and electrical applications.[18] Bismuth structural behavior in non-crystalline materials is complicated since it differs from the usual purpose of glass making. The incorporation of Bi^{3+}ions into the glass network introduces BiO_3 pyramidal structural units and [BiO_5/BiO_6] polyhedral units, facilitated by the high polarizability and large ionic radius of bismuth.[19] Glass-based dielectrics are important for power electronics because they can operate at high temperatures where many polymers fail. Glass materials can be recycled and re-melted, which supports long-term sustainability goals in electronics manufacturing. Heavy metal-containing glasses are still investigated because they offer strong dielectric performance that is useful for demanding applications, even though environmental concerns require future mitigation or substitution.

Glass and ceramic materials were among the first to be used in commercial electronic applications, particularly in low-dielectric components. The non-crystalline substances with a great concentration of alkalis and heavy metal ions are members of the fast ionic conductivity (FIC) family of materials.[20] Thus, it is important to investigate ionic mobility in glass structures and to explore novel glass materials for use as potential electrode and electrolyte materials. The dielectric properties of glass materials are reflected in the movement of ions in the glass structure, ion hopping from low-energy to high-energy sites, and electron hopping between ions of multivalent elements.[21,22] The dielectric characteristics of bismuth-containing glass and impedance spectroscopy revealed that a dipolar relaxation effect caused by an increase in the concentration of Bi_2O_3 in the host glass causes a consistent drop in the frequency-dependent conductivity of these glasses.[23] A lot of work has been done to understand the electrical and structural properties of Bi_2O_3-based glasses. Many studies investigated the impact of Bi_2O_3 addition as a glass former or modifier on the dielectric behavior and polarization mechanisms.[23–26] Bi_2O_3 (bismuth oxide) addition to glass systems can alter their dielectric characteristics, and its influence is governed by several factors such as glass composition and present oxide components. Bi_2O_3 addition to K_2O–TiO_2–P_2O_5 glass systems leads to increased dielectric constant and decreased dielectric loss, with a favorable impact on permittivity.[25] Dielectric dispersion at low frequency is decreased by Bi_2O_3 addition, with better dielectric stability in frequency ranges. Li_2O– Bi_2O_3–TeO_2–Ag glasses exhibit nonlinear conductivity and dielectric response with Bi_2O_3 composition, reflecting initial loss with subsequent improvement in dielectric constant with the increase in Bi_2O_3 content, with implications of compositional complexities.[27] In Na_2O–CuO–SiO_2, Li_2O–Bi_2O_3–B_2O_3–As_2O_3 glass systems, higher Bi_2O_3 content reduces AC conductivity. This is because Bi_2O_3 promotes network polymerization and its electronegative nature suppresses ionic movement. The electrical characteristics of bismuth silicate glasses were examined by Kusz *et al.*,[28] who found that the conductivity of the prepared materials results from a single ionic process, and is dependent on the mobility path of Bi^{3+} ions. Bi_2O_3 plays a more intricate and poorly understood structural role in oxide glasses. This is because the presence of lone-pair electrons causes the [BiO_n] polyhedra to be extremely deformed. There are few reports on the dielectric properties of cadmium-silicate glasses, and even fewer studies that discuss the effect of bismuth oxide on the dielectric properties of such glass systems. There are still a lot of unresolved issues about the structure and conductivity mechanism of glass materials. Therefore, the goal of the present research is to create new Bi_2O_3-containing glasses based on the composition of $(60 - X)$CdO–$X$$Bi_2O_3$–40$SiO_2$ (where $X = 0$, 7.5, 15 and 30 mol%) and to investigate the influence of Bi_2O_3 on the structural, physical, and mechanical properties and the dielectric measurements of permittivity, dielectric loss, and AC conductivity from 0.1 Hz to 10 MHz at 30 °C–150 °C. The study also aims to correlate the structural and mechanical changes with the observed dielectric behavior.

2 Experimental

2.1 Glass creates a process

Cadmium silicate containing Bi_2O_3 with the nominal composition of $(60 - X)$CdO–$X$$Bi_2O_3$–40$SiO_2$ (where $X = 0$, 7.5, 15, and 30 mol%) was synthesized using a melt-quenching method. The compositions of the synthesized vitreous specimens are detailed in Table 1. An electronic digital LCD weighing balance (FA1004E) with an accuracy of 0.0001 g was used to precisely weigh various amounts of high-purity chemical reagents, including $CdCO_3$, Bi_2O_3, and quartz. To make a 40 g batch, a mixture of powders was meticulously weighed based on their chemical compositions. Then, in an agate mortar, the mixture powders were mixed and ground very gently for 45 minutes. To make a consistent mixture of vitreous specimens, the resultant combinations were heated to 800 °C for 60 minutes, which caused the carbonate to thermally break down into oxides and

Table 1 Composition of the investigated glasses

	Composition (mol%)			
Sample ID	CdO	Bi_2O_3	SiO_2	Melting temperature (°C)
CSB0	60	0.0	40	1375
CSB7.5	52.5	7.5	40	1325
CSB15	45	15	40	1300
CSB30	30	30	40	1250

carbon dioxide. For 90 minutes, the glass batches were placed in alumina crucibles to melt at a temperature of 1375–1250 °C. Molten amorphous materials were decanted over stainless steel molds heated to 400 °C to produce glass samples of various shapes. To release the strain, the prepared glass was annealed for two hours at 400 °C before being allowed to cool to room temperature.

2.2 Glass characterization techniques

To ascertain the amorphous nature of the samples, an X-ray diffractometer (PANalytical PW3040/60, Netherlands) equipped with a Cu-Kα radiation source ($\lambda = 1.5406$ Å) was used at 35 mA and 40 kV. The data were collected at room temperature in the 2θ range of 5°–80°, with a scan rate of 1°/min. A VERTEX 70, FT/IR-430 spectrometer was used to measure the internal structure. The FT-IR absorption spectra were recorded at ambient temperature in the wave number range of 400–1600 cm^{-1}. Using distilled water as a soaking fluid and the Archimedes technique, the bulk density of the synthesized non-crystalline materials was determined at room temperature. To ensure the accuracy of density readings, five glass samples free of flaws such as cracks and air bubbles were selected to take the average readings. The density of glass ρ was obtained using eqn (1):[29,30]

$$\rho = \left(\frac{D_a}{D_a - D_w}\right) \times \rho_w \quad (1)$$

where D_a and D_w denote the weight of the glass sample measured in air and in water, respectively, whereas ρ_w is the density of water (1 g cm^{-3}). The molar volume (V_m) for the synthesized samples was obtained using eqn (2):[31,32]

$$V_m = M_{wt}/\rho \quad (2)$$

where M_{wt} is the molecular weight of the whole glass system, calculated as the sum of the products of each oxide's mole fraction and its respective molecular weight. The oxygen packing density (OPD) of the synthesized samples was calculated using eqn (3):[31,32]

$$OPD = 1000T/V_m \quad (3)$$

where T is the total oxygen present in each oxide glass constituent. The value of oxygen molar volume (V_O) was obtained using eqn (4):[31,32]

$$V_O = V_m/(\sum x_i n_i) \quad (4)$$

where x_i is the molar fraction and n_i is the number of oxygen atoms present in each oxide, respectively.

2.3 Mechanical study by elastic modulus calculation

The primary challenge in the Makishima–McKenzie principle is the use of the following relations to determine the total ionic packing density (V_t) and the total dissociation energy per unit volume (G_t) for the glass system oxides:

$$V_t = (1/V_m)\sum_i V_i x_i \quad (5)$$

$$G_t = \sum_i G_i x_i \quad (6)$$

The packing density factor (V_i) and the dissociation energy per unit volume of the supplied glass system oxides (G_i) are represented by these variables.[33–35] The samples' elastic modulus was designed to theoretically extend the Makishima–McKenzie model.[36,37] The following formulae are used to measure the elastic parameters:[36,37]

$$E = 2V_t G_t \quad (7)$$

$$B = 1.2V_t E \quad (8)$$

$$S = 3EB/(9B - E) \quad (9)$$

$$L = B + \left(\frac{4}{3}\right)S \quad (10)$$

$$\sigma = 0.5 - (1/7.2V_t) \quad (11)$$

where E is Young's modulus, B is the bulk modulus, S is the shear modulus, L is the longitudinal modulus, and σ is Poisson's ratio.

2.4 Dielectric study

A BA broadband dielectric spectroscopy system fitted with a high-precision Alpha-A analyzer was used for dielectric measurements at frequencies between 0.1 Hz and 10 MHz and temperatures starting from 30 °C with a step of 20 °C up to 150 °C with a nitrogen heating medium (Concept 40, Novocontrol Technologies).

3 Result and discussion

3.1 Vitreous synthesis and physical parameters

The amorphous nature of the synthesized $(60 - X)$CdO–$X$$Bi_2O_3$–40$SiO_2$ glasses was confirmed by X-ray diffraction analysis. Patterns of CSB0 and CSB30 are shown in Fig. 1 as representative examples for the series.

The presence of a typical "halo" pattern at $20° \leq 2\theta \leq 30°$ without any prominent peaks in the XRD measurements throughout a range of 10°–80° proved the samples' amorphous nature. The absence of distinct peaks confirms that the prepared samples are amorphous or non-crystalline materials.[7,38] Information obtained from prepared materials, such as physical properties, is an important foundation upon which their possible use in numerous technological applications is based. Measurements of density (ρ), molar volume (V_m), oxygen packing density (OPD), and oxygen molar volume (V_O) were used to examine the basic physical characteristics of the synthesized glass materials. The ρ and V_m variations of the synthesized samples are presented in Fig. 2. The results show that the substitution of cadmium oxide by Bi_2O_3 increases the density of the non-crystalline materials. The density of CSB30 is found to be 6.45 g.cm^{-3}, which is higher than the density obtained for

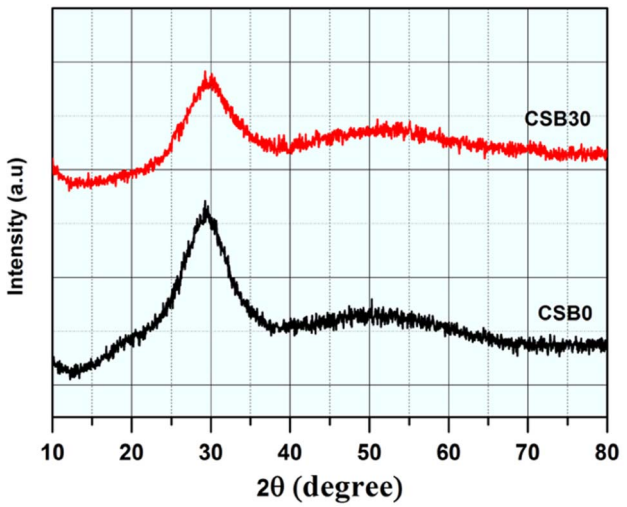

Fig. 1 XRD patterns of the Bi_2O_3 modified $CdO–SiO_2$ glass samples CSB0 (Bi_2O_3-free) and CSB30 (with 30 mol% Bi_2O_3).

base glass CSB0 (5.73 g.cm^{-3}). The density increases due to the substitution of the CdO compound (molar mass of 128.4112 g mol^{-1}) with the Bi_2O_3 oxide (molar mass of 465.96 g mol^{-1}), leading to an increased molecular mass (M) of the samples.[39] The connection between the density and the molar volume is mostly inverse. However, in certain cases, the relationship is directly related under special conditions.

Fig. 2 shows that V_m rises in conjunction with the inclusion of Bi_2O_3 instead of CdO from 17.64 cm^3 mol^{-1} for the Bi_2O_3-free sample to 30.42 cm^3 mol^{-1} for the sample that has a lot of bismuth (30 mol%). The increases in molar volume reflect the formation of BiO_3 pyramids and BiO_6 octahedra.[40,41] The integration of Bi^{3+} ions into the glass network through Bi–O–Si and Bi–O–Bi linkages indicates the growth of the glass structure.[40,41]

The increase in V_m with substitution reinforces the fact that the addition of Bi_2O_3 reduces the cohesion and compactness of the glass structure.[36,42] The data in Fig. 3 indicate a decrease in OPD and an increase in V_O as the concentrations of Bi_2O_3 increase. The OPD of the glass samples varied between 79.363 and 65.729 mol cm^{-3}, and the V_O values varied from 12.60 to 15.21 cm^3 mol^{-1}. The decrease in the OPD and the increase in volume with increasing Bi_2O_3 concentration indicate that a higher non-bridging oxygen content leads to bond lengthening and reduced network compactness, weakening the glass network strength. These structural changes in molar volume, oxygen packing density, and network compactness are further reflected in the mechanical properties and dielectric responses discussed in the following sections.

3.2 Glass structure (FTIR)

It is very important to study and verify the structural composition of the synthesized vitreous specimen because it reflects and explains the properties of the produced materials. The structural arrangement of glassy materials depends on the properties of the cations present in the compositions and the role of those cations in modifying the glass network. Structural changes occurring due to the addition of Bi_2O_3 instead of CdO in the cadmium silicate network are investigated by FTIR spectra analysis (Fig. 4). The FTIR absorbance spectra arising from the vibrations of the cadmium bismuth silicate network are documented at room temperature within the frequency range of 400–1600 cm^{-1}, as shown in Fig. 4. The FTIR spectrum shows that there are two main absorption areas in the 600–1200 cm^{-1} and 400–600 cm^{-1} regions, as shown in Fig. 4. Because some regions of the FTIR spectra appear broad due to the overlap of more than one closely spaced peak, these peaks had to be separated from each other by deconvolution to know the precise values of the peaks, as shown in Fig. 4. In the base glass (free of Bi_2O_3), bands with the highest

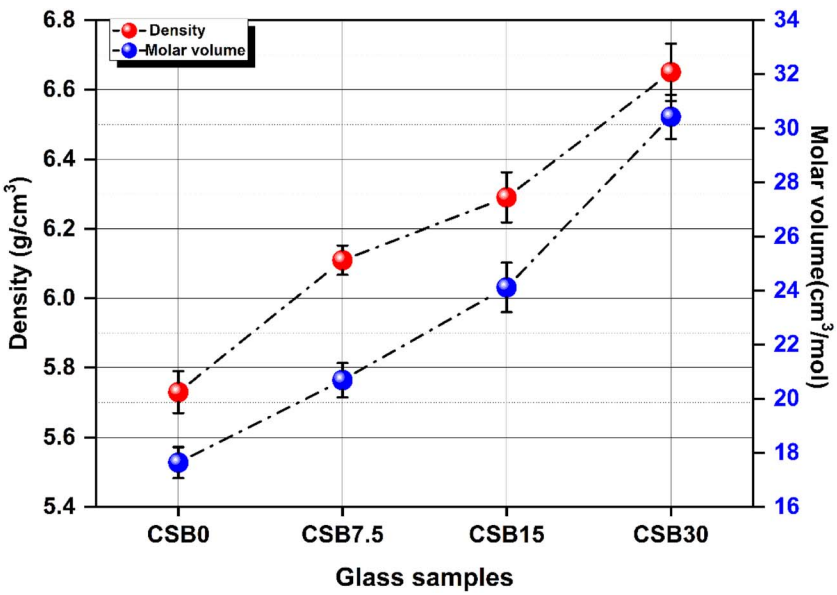

Fig. 2 Densities (ρ) and molar volumes (V_m) of the Bi_2O_3-modified $CdO–SiO_2$ glass samples *vs.* the Bi_2O_3 level.

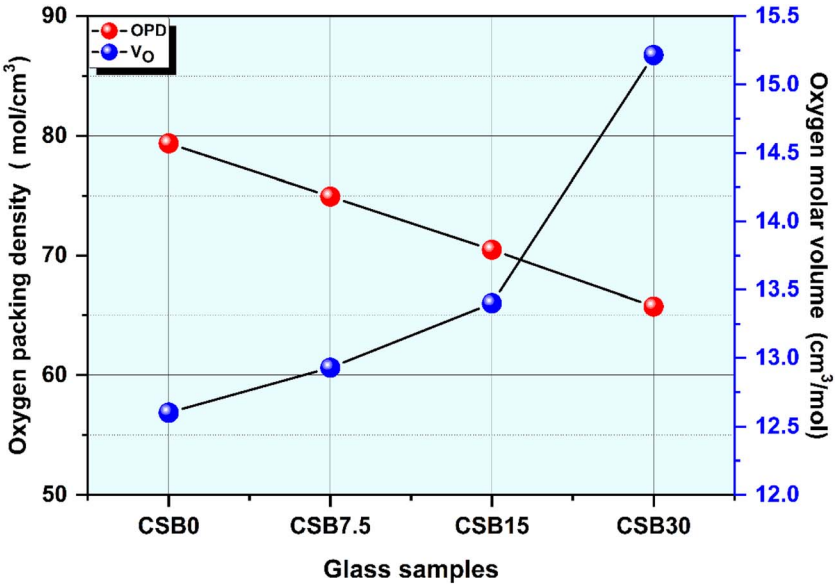

Fig. 3 OPD and V_O for the Bi_2O_3-modified $CdO–SiO_2$ glass samples *vs.* the Bi_2O_3 level.

density are located between 400 and 600 cm^{-1}, followed by the second band between 800 and 1200 cm^{-1} which are typical of silicate glasses.[43] The Si–O–Si asymmetric stretching of BOs is responsible for the absorption band at 1028 cm^{-1} in the high-frequency range (800–1200 cm^{-1}).[43,44]

The absorption at 927 cm^{-1} is attributed to the Si–O asymmetric stretching vibrations in Q^2 structural units containing two non-bridging oxygens per SiO_4 tetrahedron. The band at 870 cm^{-1} is consistent with NBO-related Si–O vibrations in modifier-affected silicate environments.[45,46] The ν_s(Si–O–Si) bending vibration is responsible for the weak absorption band that is displaced from 765 cm^{-1}. The wide absorption band centered at about 439 cm^{-1} can be attributed to the δ(O–Si–O) bending vibration mode.[47] From the infrared results studied, a difference was found in the strength of the band between 700 and 1200 cm^{-1}, especially at the peak of 857 cm^{-1}, with a decrease in the intensity of the band between 400 and 600 cm^{-1} with the inclusion of bismuth instead of cadmium. This band evolution indicates BiO_6 octahedral formation and Si–O–Si bond disruption, which would weaken the strength of the glass network. The 860–880 cm^{-1} enhancements indicate BiO_3 pyramidal units, reducing cross-link density and rigidity of the glass.[18,36,48] Tetrahedral coordinated oxygen (SiO_4) can change into three-coordinated non-bridging oxygen (NBO) species (Q^3) when bismuth oxide (Bi_2O_3) is added. This change creates oxygen vacancies, reducing structural coherence.

The deconvoluted FTIR spectra for CSB0 and CSB30 are presented in Fig. 4b and c. For CSB0, deconvolution yields seven components at 1028, 927, 870, 765, 672, 484, and 439 cm^{-1}. The band at 1028 cm^{-1} is assigned to the Si–O–Si asymmetric stretching vibrations associated with bridging oxygen environments in the silicate network. The band at 927 cm^{-1} is attributed to the Si–O stretching vibrations in Q^2 structural units containing two non-bridging oxygens per SiO_4 tetrahedron. The band at 870 cm^{-1} is consistent with NBO-related Si–O vibrations in modifier-affected silicate environments. The band at 765 cm^{-1} corresponds to the ν_s(Si–O–Si) bending vibrations. The bands at 672 and 484 cm^{-1} are assigned to Cd–O vibrations, while the band at 439 cm^{-1} is attributed to δ(O–Si–O) bending. In CSB30, the components appear at 1041, 946, 857, 672, 606, and 462 cm^{-1}. The shift of the 1028 cm^{-1} band to 1041 cm^{-1} suggests changes in the Si–O bond environment associated with network modification. The shift of the 927 cm^{-1} band to 946 cm^{-1}, together with the enhanced intensity in the NBO-related region, suggests an increased fraction of non-bridging oxygens as Bi_2O_3 replaces CdO. The dominant band at 857 cm^{-1} is consistent with Bi–O vibrations commonly associated with BiO_3 pyramidal units in bismuth-containing glasses. The new band at 606 cm^{-1} can be attributed to the Bi–O stretching vibrations reported for octahedral coordinated Bi environments. These spectral features suggest that Bi^{3+} ions are incorporated into the glass network through Bi–O structural units consistent with BiO_3 and BiO_6 configurations rather than acting solely as interstitial modifiers. The low-frequency band shifts from 439 cm^{-1} in CSB0 to 462 cm^{-1} in CSB30 reflect changes in the Si–O bending environment accompanying structural rearrangement of the glass network. This progressive increase in the non-bridging oxygen content is independently supported by the observed rise in molar volume from 17.64 to 30.42 cm^3 mol^{-1}, the decrease in oxygen packing density from 79.363 to 65.729 mol cm^{-3}, and the reduction in elastic moduli and microhardness, collectively indicating progressive network depolymerization that governs the dielectric and electrical response of the glasses.

3.3 Elastic modulus factors and microhardness

The Makishima–McKenzie model was selected for this study because it is well established for oxide glass systems and

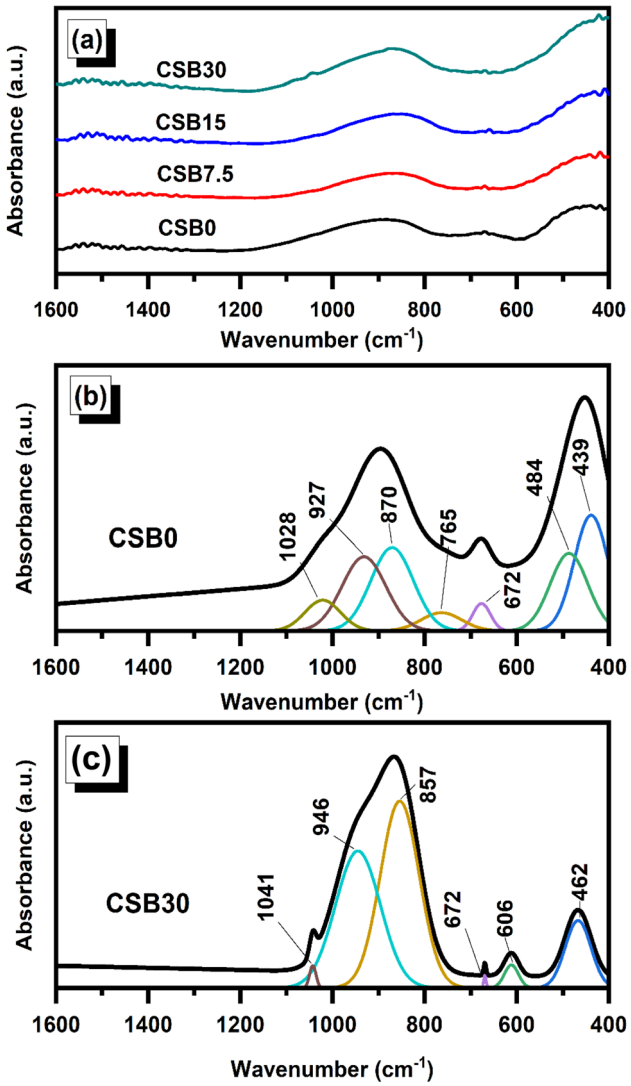

Fig. 4 FTIR absorbance spectra of all four Bi_2O_3-modified CdO–SiO_2 glass samples (a) and deconvoluted FTIR spectrum of glass samples: CSB0 (b) and CSB30 (c).

requires only the ionic packing density and dissociation energy of each constituent oxide as inputs, both of which are available for CdO, Bi_2O_3, and SiO_2. This model has been successfully applied to similar heavy metal oxide glass systems containing bismuth and cadmium, validating its suitability for the present glass composition.[49–51] The calculated elastic moduli of the prepared non-crystalline materials, such as Young's modulus (E), bulk modulus (B), shear modulus (S), and longitudinal modulus, are presented in Table 2 and Fig. 5. The elastic modulus parameters for the vitreous samples are as follows: the E value varied between 59.406 and 49.633 GPa, the B value varied from 44.938 to 31.690 GPa, the S value varied from 23.212 to 20.030 GPa, and the L value varied between 75.887 and 58.397 GPa. The analysis of the results indicates that the elastic modulus parameters exhibit a decrease with the incorporation of Bi_2O_3 in place of CdO, as illustrated in Fig. 5 and Table 2. The results of the oxides' dislocation energy were used to compute the elastic moduli. The decrease in dislocation energy may be responsible for the reduction in elastic modulus parameters. Bi_2O_3 lowers the dissociation energy (31.6 kJ cm^{-3}) to some extent in comparison to CdO (33.2 kJ cm^{-3}), which could be the cause of the dissociation energy.[52] The reduction in elastic moduli is associated with a decrease in network connectivity due to the formation of BiO_3 structural units, which introduce lower cross-link density compared to the original Cd–O network.[36]

The relationship between the atomic packing density and the Poisson ratio is depicted in Fig. 6, according to Bi_2O_3 and CdO contents. The findings revealed a decrease in both the atomic packing density and the Poisson ratio with CdO substitution by Bi_2O_3 and an increase in molar volume, which confirms the precision of the mechanical parameter computations. The Poisson ratio and the atomic packing density are directly related.[53] There was greater room for atom movement as a result of the reduction in both the Poisson ratio and the atomic packing density, and transverse strain could be minimal.[44]

Micro-hardness is an essential mechanical property that manufactured materials must possess since it significantly affects the choice of appropriate technological applications. The experimental Vickers micro-hardness (H_v) values and Poisson's ratio (σ) of the prepared glass specimens as a function of Bi_2O_3/CdO is shown in Fig. 7. When the values fall between 0.3 and 0.5, σ shows low resistance to lateral expansion; when the values fall between 0.1 and 0.2, the resistance is stronger. High and low real cross-link densities are associated with low and high resistances to lateral expansion, respectively.[54] Increased NBO formation reduces network stiffness, decreasing H_v and σ.[36,38] According to Fig. 7, the microhardness of samples presents a linear trend decreasing with the progress of CdO substitution by Bi_2O_3. The decrement in H_v from 5.86 to 3.87 GPa with the increase in Bi_2O_3 attributed to the creation of NBO and the formation of BiO_3 groups to decrease the toughness of the network. The decrease in H and σ indicates increased formation of non-bridging oxygens, resulting in a less rigid and more

Table 2 Calculated and experimental parameters of the investigated glasses

Sample ID	Poisson's ratio (σ)	Atomic packing density (V_t)	Dislocation energy (G_i)	Elastic moduli parameters (GPa)				Experimental microhardness HV (GPa)
				E	S	L	B	
CSB0	0.27967	0.630374	47.12	59.406	23.212	75.887	44.938	5.86
CSB7.5	0.26807	0.59884	47.01	56.291	22.196	70.060	40.451	5.13
CSB15	0.25467	0.566141	46.88	53.081	21.153	64.266	36.062	4.50
CSB30	0.23897	0.532081	46.64	49.633	20.030	58.397	31.690	3.87

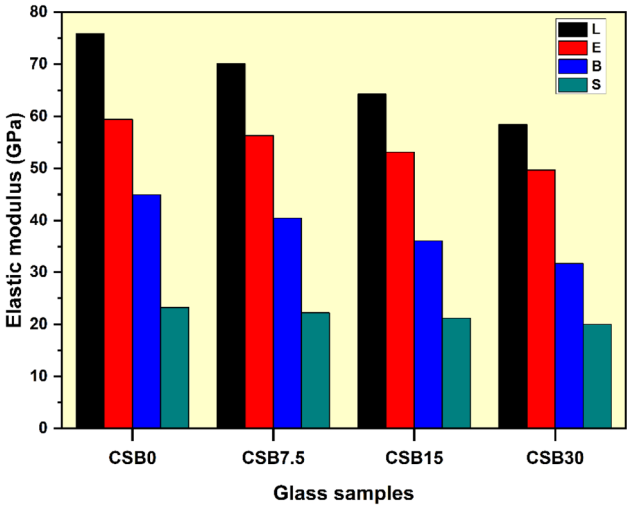

Fig. 5 Estimated mechanical characteristics, including the longitudinal (*L*), bulk (*B*), shear (*s*), and Young's (*E*) moduli, *vs.* the Bi_2O_3 level.

weakly connected glass network. This reduction in mechanical stiffness is consistent with the FTIR-based evidence for increased non-bridging oxygen content and BiO_3 unit formation, as well as the rise in molar volume and decrease in oxygen packing density observed with the increase in Bi_2O_3 content.

3.4 Dielectric study

3.4.1 Dielectric permittivity. The permittivity (ε') as a function of frequency for the four compositions CSB0, CSB7.5, CSB15, and CSB30 is demonstrated in Fig. 8 at temperatures between 30 and 150 °C. The lowest overall permittivity among all of the compositions belongs to CSB0 and is approximately 18–27. The temperature dependence of sample CSB0 and its frequency dispersion are both low compared to other compositions across the entire frequency span. ε' is approximately 20 at 30 °C and ~27 at 150 °C at the lowest frequency (0.1 Hz). All curves approach 18–20 at frequencies above 100 Hz, where ε' decreases slightly as the frequency is higher. The permittivity of the CSB7.5 sample is in the range of ~17–45, and is much higher than that of CSB0. Frequency dependence is strong, especially at higher temperatures. ε' goes down from ~45 at 0.1 Hz to ~35 at 10 MHz as the temperature is 150 °C. ε' goes down from ~32 at 0.1 Hz to ~17 at 10 MHz at 30 °C. Especially in the temperature range of 100–150 °C, distinctive step-like drops of ε' can be seen between 10^2 and 10^5 Hz. Temperature curves at high temperatures are more frequency dependent and tend to have clear separation among the temperature curves across the frequency range.

CSB15 shows further permittivity increase (17–55), particularly at low frequency, with strong frequency dependence, especially at high temperatures. ε' goes down from ~5 at 0.1 Hz to ~23 at 10 MHz at 150 °C. ε' goes down from ~35 at 0.1 Hz to ~17 at 10 MHz at 30 °C. Fast relaxation behavior can take the form of sharp drops in ε' at mid-frequencies. When the temperature goes higher, relaxation moves to a higher frequency. At high frequency (>1 MHz), all temperature curves are approximately close to 17–21. CSB30 exhibits the highest permittivity (24–65). The maximum ε' at 0.1 Hz and 150 °C is ~65, the highest in all the compositions. ε' is close to 36 at 0.1 Hz and 30 °C. It also has high temperature and frequency dependence along with the well-defined relaxation behavior much like CSB15 but with a higher magnitude.

The curves for the various temperatures are well resolved from each other at all high-frequency situations. ε' varies between ~24 (30 °C) and 30 (150 °C) at 10 MHz. An increase in the concentration of Bi_2O_3 gradually leads to an increase in the dielectric permittivity.[55] The maximum ε' at 0.1 Hz and 150 °C has the following order: CSB0 (~27) < CSB7.5 (~45) < CSB15 (~55) < CSB30 (~65). The dielectric relaxation enhances with

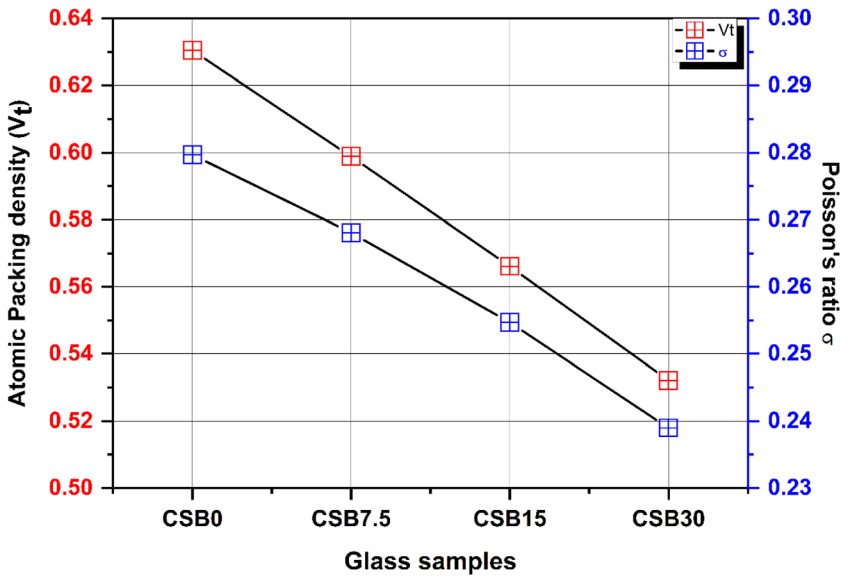

Fig. 6 Atomic packing density (V_t) and Poisson's ratio (σ) *vs.* the Bi_2O_3 level.

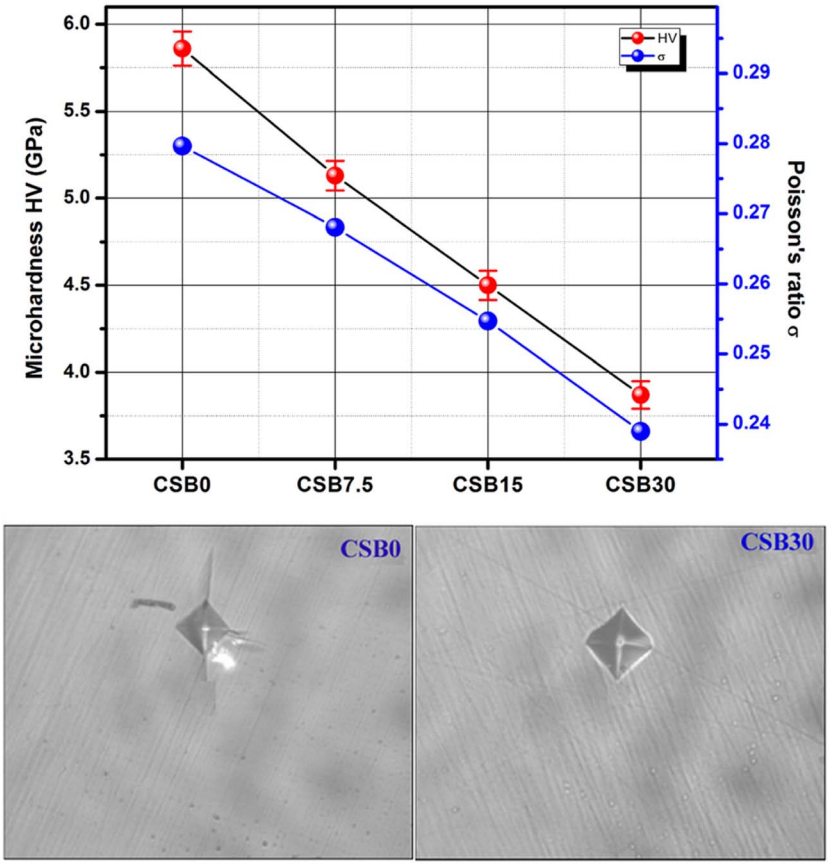

Fig. 7 Variation of Vickers micro-hardness (H_v) and Poisson's ratio (σ) of the prepared glass specimens as a function of Bi_2O_3 content.

the increase in the concentration of Bi_2O_3. Dielectric permittivity becomes more dependent on temperature with an increasing ratio of Bi_2O_3 in the material. The temperature effect gets higher for the increasing concentration of Bi_2O_3, and its effect is highly noticed at low frequencies, which vanishes at high frequencies. With increasing frequency, ε' decreases for all compositions, and the extent of dispersion becomes more pronounced as the Bi_2O_3 content increases. With increasing temperature, the relaxation region, marked by the sharp decrease in ε', shifts toward higher frequencies, with the main dispersion occurring in the 10–10^5 Hz range depending on composition. CSB7.5 shows an almost plateau-like behavior at very low frequencies (0.1–10 Hz), more prominent in the higher temperature curves (100–150 °C). At 150 °C, ε' is in the range of 44–45 between 0.1 and 1 Hz before it starts decreasing more steeply. A similar near-saturation type of behavior in CSB15 is observed at low frequencies where ε' is around 53–55 between 0.1 and 1 Hz at 150 °C. At frequency values above 10 Hz, the permittivity has a well-defined and rather steep decline. The effect gets augmented by increasing both the temperature and the concentration of Bi_2O_3.

At frequency values above 10 Hz, the permittivity has a well-defined and rather steep decline, which suggests some specific mechanisms of polarization becoming operative at the involved frequency. SiO_2 has low polarizability ($\varepsilon' \approx 3.9$). CdO introduces highly polarizable heavy ions, resulting in ε' values in the range of approximately 18–27 for the CSB0 composition. The closed-shell $4d^{10}$ configuration of Cd^{2+} ions enhance electronic polarizability, while its role as a network modifier promotes the formation of non-bridging oxygens (NBOs) that enable ionic displacement under an applied field. However, the relatively intact silicate network in CSB0 limits NBO formation, and hence, the response remains largely dominated by electronic polarization, as reflected by the weak frequency and temperature dependence above ~100 Hz. CSB0 therefore represents a baseline electronic polarization response against which the effects of Bi_2O_3 addition can be evaluated. CSB0 shows little change with temperature or frequency. Above 100 Hz, ε' approaches a constant value as the response becomes dominated by electronic polarization. Adding 7.5 mol% Bi_2O_3 increases ε' to 17–45. Bi–O units and non-bridging oxygens boost space-charge polarization.[25,55] At 100–150 °C, ε' drops in steps between 10^2 and 10^5 Hz. A low-frequency plateau appears at 0.1–1 Hz and 150 °C. Temperature curves separate more with Bi_2O_3, showing stronger thermal activation. CSB15 reaches an ε' value of 17–55. More BiO_3/BiO_6 units enhance the local dipolar polarizability within the glass network.[25,56] Mid-frequency drops shift to higher frequencies as the temperature increases. All curves converge to similar ε' values (17–21) above 1 MHz, consistent with high-frequency polarization dominated by intrinsic electronic contributions.[57] All compositions (CSB0–CSB15) converge to similar ε' values (≈17–21) above 1 MHz,

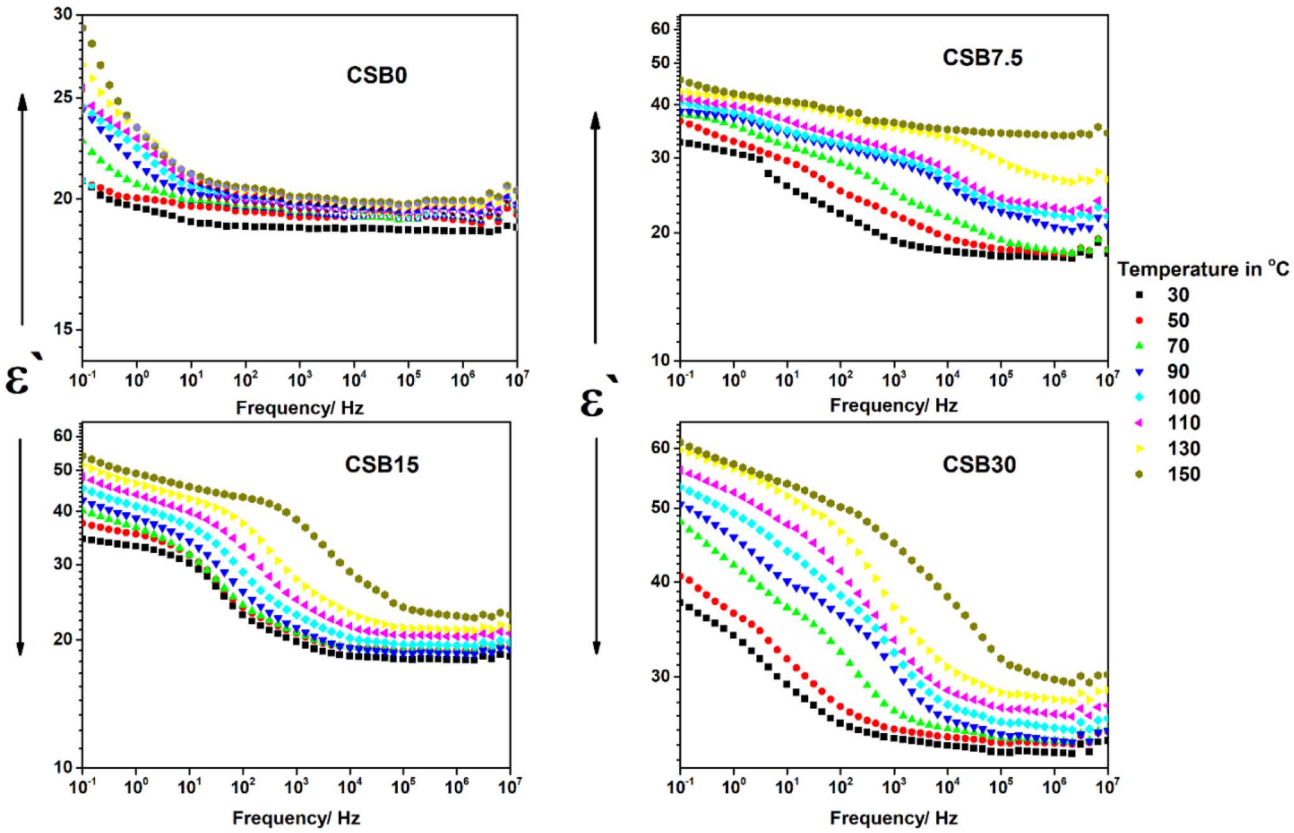

Fig. 8 Dielectric permittivity *vs.* frequency the for Bi_2O_3-modified CdO–SiO_2 glasses, at temperatures between 30 and 150 °C with a step of 20 °C as indicated.

consistent with the dominance of intrinsic electronic polarization associated with Cd^{2+} within the Si–O and Cd–O bonding framework. At a higher Bi_2O_3 content (CSB30), the increased concentration of Bi^{3+} ions with 6 s^2 lone-pair electrons provides additional electronic polarizability, leading to a noticeable rise in the high-frequency ε' ($\approx$23–30). This behavior suggests that heavy cations with ns^2 electronic configurations can further enhance the electronic component of the dielectric response. CSB30 has the highest ε' of 24–65. Relaxation shifts to a higher frequency with more Bi_2O_3 and higher temperatures. ε' always falls as the frequency increases. The high-frequency ε' remains nearly constant at ~18 for samples with up to 20 mol% Bi_2O_3, then increases in CSB30, because at these frequencies the dielectric response is dominated mainly by electronic polarization. Up to 20 mol% Bi_2O_3, adding Bi causes network expansion but does not change the core electronic polarizability much. The Si–O and Cd–O bonds still dominate the response at >1 MHz, holding ε' near 18. At 30 mol% Bi_2O_3, the concentration of Bi^{3+} ions with their 6 s^2 lone pairs becomes high enough to boost the electronic polarizability of the glass.[48,49] These Bi–O units add extra polarizable electrons that can follow the high-frequency field, increasing ε' to about 23.

Network expansion from CdO substitution by Bi_2O_3 increases the molar volume and lowers the packing density. More free volume means that the oxygen ions can shift more under a field. The extra motion boosts low-frequency ε' because dipoles and space charge polarize easily. FTIR spectra show the growing non-bridging oxygen (NBO) content as the Bi_2O_3 content rises. Each NBO breaks a Si–O–Si bond and creates a more polarizable site. More NBOs correlate with higher ε' at low and mid-frequencies, since those oxygens can reorient or trap charges in slower fields. Mechanical moduli drop (E, B, S, and L) and hardness falls with Bi_2O_3 addition. This means that the network becomes softer with a lower restoring force, which indicates a possible increment of dipolar polarization at low frequencies.[48,56] Weaker networks allow dipoles to follow fields more before high frequencies.

3.4.2 AC conductivity. The AC conductivity of the four samples is manifested in Fig. 9. All samples have near-values at low frequencies (0.1 Hz to 10 Hz), while the neat sample has relatively low values. The CSB0 sample at low frequencies (0.1 Hz to 10 Hz) possesses conductivity with very low values, and it rises steadily with frequency and temperature. Only at 130 °C and 150 °C does conductivity stop increasing with frequency below about 1 Hz, forming a clear plateau. In the range of frequencies (10 Hz to 100 kHz), conductivity follows a smooth and gradual slope upward, which steepens with the increase in frequency. The conductivity values at 0.1 Hz are 3.51 $\times$ 10^{-14} S cm^{-1} (at 30 °C) and 2.9 $\times$ 10^{-12} S cm^{-1} (at 150 °C). Temperature curves stay spread out at low frequencies, but they come close together past about 100 Hz. Above 1 MHz, all temperature curves converge and rise sharply, with the

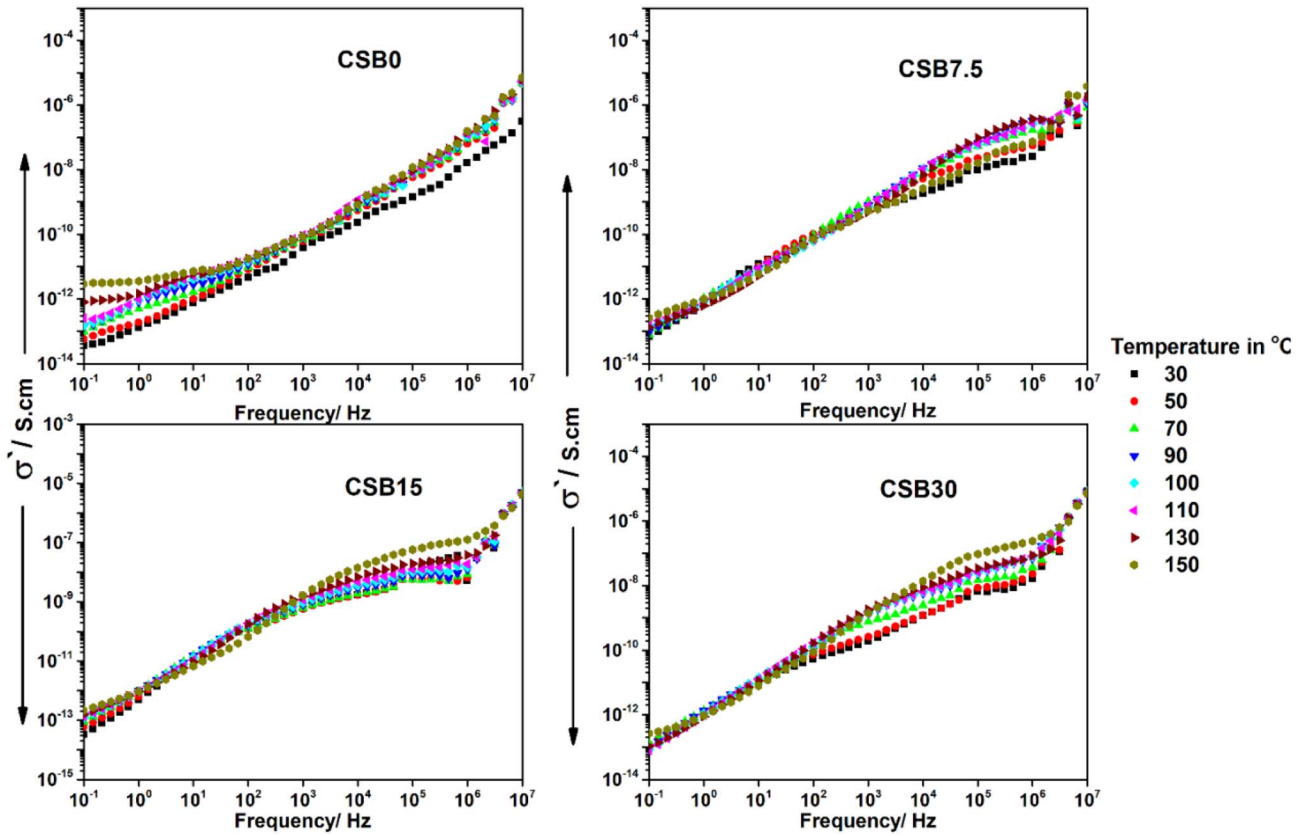

Fig. 9 AC conductivity (σ') *vs.* frequency for the Bi_2O_3-modified CdO–SiO_2 glasses at temperatures between 30 and 150 °C with a step of 20 °C as indicated.

conductivity increasing by several orders of magnitude at 10 MHz. CSB7.5 sample's conductivity rises gradually for all temperatures at low frequencies (0.1 Hz to 10 Hz), and no flat plateau is observed. Conductivity at 150 °C and 0.1 Hz is two orders of magnitude higher than that at 30 °C. In the mid-frequency region (10 Hz to 10 kHz), conductivity has a steeper slope than that of CSB0. At high frequencies (1 MHz to 10 MHz), all temperature curves rise sharply and converge near the same value. Above 10 kHz, the ε' curves at different temperatures are separated by approximately two to three decades. CSB15 sample's conductivity curves begin to fan out at an earlier frequency (about 1 KHz), with higher temperatures showing a higher conductivity. The conductivity grows faster with the frequency and temperature. At frequencies above 1 MHz, the curves get closer, but high-temperature curves stay slightly above low-temperature curves. The slope is steeper, showing stronger dispersive conduction. The CSB30 conductivity values rise faster with temperature. There is no flat region at low frequencies, and curves spread above 100 Hz, earlier than other samples. At frequencies ≥1 MHz, all curves collapse toward a common value. The slope from 1 MHz to 10 MHz is the steepest of all compositions, showing the highest contribution from electronic or displacement currents.

The conductivity increases monotonically with frequency in three regions. From 0.1 Hz to 10 Hz, the slope is gentle. From 10 Hz to 100 kHz, the slope becomes moderate with higher Bi_2O_3 contents and higher temperatures. From 1 MHz to 10 MHz, the slope is steep and all temperatures converge. A semi-peak feature appears in all doped samples and has two shifts: one to higher frequencies as the temperature rises and another to lower frequencies as the Bi_2O_3 content increases. Slope steepness in the mid-frequency region increases with the Bi_2O_3 content: CSB0 is the shallowest, and CSB30 is the steepest. At any fixed frequency, conductivity always rises with temperature. The separation between the 30 °C and 150 °C curves is small at low frequencies (except for CSB0 at its highest temperatures) and largest in the frequency range of 100 Hz to 1 MHz. Above 1 MHz, the temperature dependence weakens slightly as electronic polarization takes over.

CSB0 glass network is tight and has few non-bridging oxygens. At low frequencies below 1 Hz, the conductivity keeps rising until 130 °C and 150 °C, where it flattens into a DC-like plateau. The FTIR spectrum shows strong Si–O–Si bands; this indicates a well-connected silicate network. This leads to fewer non-bridging oxygens (NBOs) and limited dipolar or ionic polarization mechanisms. The CSB0 glass network is relatively compact and contains a limited concentration of non-bridging oxygens. Although CdO contributes to both electronic and ionic polarization mechanisms, the ionic component remains limited in CSB0 due to restricted NBO formation and the relatively high network rigidity, consistent with the measured elastic moduli and hardness. As a result, electronic polarization

associated with Cd^{2+} dominates the dielectric response, while significant ionic conduction emerges only at elevated temperatures (≥130 °C), where thermal activation facilitates charge carrier mobility. This also explains the smooth, gradual temperature behavior permittivity (ε') that also lacks sharp features. The same structural tightness also constrains low-frequency conductivity (σ') at lower temperatures, since fewer free carriers and lower hopping likelihood exist with a tighter potential landscape. With the increase in temperature, the thermal energy allows charge carriers to cross the strong network constraint, facilitating hopping through the rigid structure. That is, when σ' rises more steeply, ε' will begin to exhibit deviations (particularly, at low frequencies) due to space charge or interfacial polarization. The lack of NBO-related signatures in the FTIR spectrum corroborates the late onset of dispersion in conductivity, and this implies that AC conductivity remains flat (DC regime) until the onset of sufficient ion mobility or polaron hopping at a later temperature. CSB0's elastic moduli and hardness are high, so carriers need $T \geq 130$ °C to reach constant low-frequency conductivity. CSB0 has no mid-frequency shoulder in σ', as the permittivity shows no sharp drop in that range. At a high frequency above 1 MHz, all show near-ε' values and rise steeply, as only electronic polarization remains. CSB7.5 adds non-bridging oxygens and Bi_2O_3 units. FTIR shows emerging Bi_2O_3 bands, so permittivity drops slightly in the 100 Hz–100 kHz range. In conductivity, a mild shoulder appears around 1 kHz, matching the permittivity relaxation. The molar volume is higher and the oxygen packing density is lower than those of CSB0, so the network is slightly softer. Elastic moduli and hardness drop a little, letting carriers move at lower frequencies. Conductivity rises earlier with the frequency but never flattens to a plateau down to 0.1 Hz. The mid-frequency slope is steeper than that of CSB0, matching the permittivity relaxation. High-frequency behavior again converges for all temperatures near the same value. CSB15 further increases non-bridging oxygens and BiO_6 groups. Permittivity has a clearer step in the 100 Hz–100 KHz band. Conductivity shows a more pronounced shoulder matching that and shifts to higher frequencies with the increase in temperature. The molar volume is larger and the oxygen packing density is lower, providing more free volume. Elastic moduli and hardness drop more, and hence, the carriers move more easily. At a high frequency above 1 MHz, all curves merge near the same value, reflecting electronic polarization.

CSB30 has the most non-bridging oxygens, the largest molar volume, and the lowest oxygen packing density. The FTIR spectrum shows dominant BiO_3/BiO_6 features and weak Si–O–Si bands, so permittivity peaks around 65 at low frequency and drops broadly in the 100 Hz–100 kHz range. Conductivity shows a strong shoulder. The network is very soft, with the lowest elastic moduli and hardness, so ion motion is easiest. The mid-frequency slope in σ' is the steepest of all samples. At a high frequency above 1 MHz, curves converge near the same value, as only electronic polarization persists.

In all doped samples, the peak or shoulder feature shifts to a higher frequency, while the spread starting point shifts to lower values with the Bi_2O_3 content. This behavior reflects a combined effect of network modification and carrier dynamics due to the increase in Bi_2O_3 content. It can be explained as follows.

3.4.2.1 The semi-peak or shoulder in σ' shifting to a higher frequency. Adding Bi_2O_3 introduces non-bridging oxygens (NBOs) and weakens the glass network; this structural disruption lowers the potential barriers for ion or polaron hopping. As a result, carriers can respond to faster oscillating fields, meaning that the hopping relaxation time becomes shorter, and the corresponding dispersion or relaxation feature in conductivity appears at higher frequencies.

3.4.2.2 Spread starting point (onset of dispersion) shifting to lower frequencies. With Bi_2O_3, the number of mobile carriers increases due to the creation of defects or localized states (NBOs, Bi sites). Even at a low frequency, more carriers start contributing to the conductivity. This means that the flat DC region ends earlier, and the frequency at which AC contribution begins starts at a lower value.

Adding Bi_2O_3 breaks some Si–O–Si bonds and creates many non-bridging oxygens. This makes the network more disordered and gives ions a lot of different local sites. Some of those sites are still tight and force ions to move very slowly. Those slow sites start to conduct at low frequencies, so the low-frequency end of the conductivity curve moves downward. At the same time, other Bi-related sites are weak and let ions move faster. Those fast sites push the main relaxation peak to higher frequencies. With the increase in Bi_2O_3 content, the molar volume increases and the packing density decreases, which facilitates ion movement. This extra free volume means that some ions can respond even under very slow fields, extending the low-frequency side of the curve. As the Bi content goes up, the number of both slow and fast sites grows. This stretches the conductivity response, so the onset of dispersion shifts to a lower frequency and the peak shifts to a higher frequency. This implies that the system is more polarizable and more conductive in a broader window of frequencies. The broadening in the distribution of relaxation times produces more stretched dispersion. It also suggests that charge carriers in Bi-rich compositions experience less localized constraints and more site availability; hence, the full conductivity profile stretches—onset comes earlier, and the relaxation peak comes sooner in the frequency scale.

3.4.3 Dielectric loss. The dielectric loss (ε'') curves *vs.* frequency at different temperatures are presented in Fig. 10. CSB0 has ε'' around 2 at 0.1 Hz and 30 °C, rising to about 41 at 150 °C. It falls steadily with the frequency and shows a feature peak that coincides with the corresponding small permittivity dispersions. The loss drops steeply with frequency and increases with temperature. CSB0 shows no distinct mid-frequency loss peak at any temperature. CSB7.5 has two peaks centered near 10 Hz and 1 KHz at 30 °C that shift to about 148 Hz and 100 KHz at 150 °C. The height and broadening of peaks increase with the temperature, and they become more separated. CSB15 exhibits a peak at 31 Hz and another shoulder at 1.48 kHz at 30 °C, which turns into a broad sharp peak centered around 4.5 kHz at 150 °C. CSB30 displays a broader peak near 1 Hz and a large shoulder at 10 kHz at 30 °C that becomes a broader peak centered around

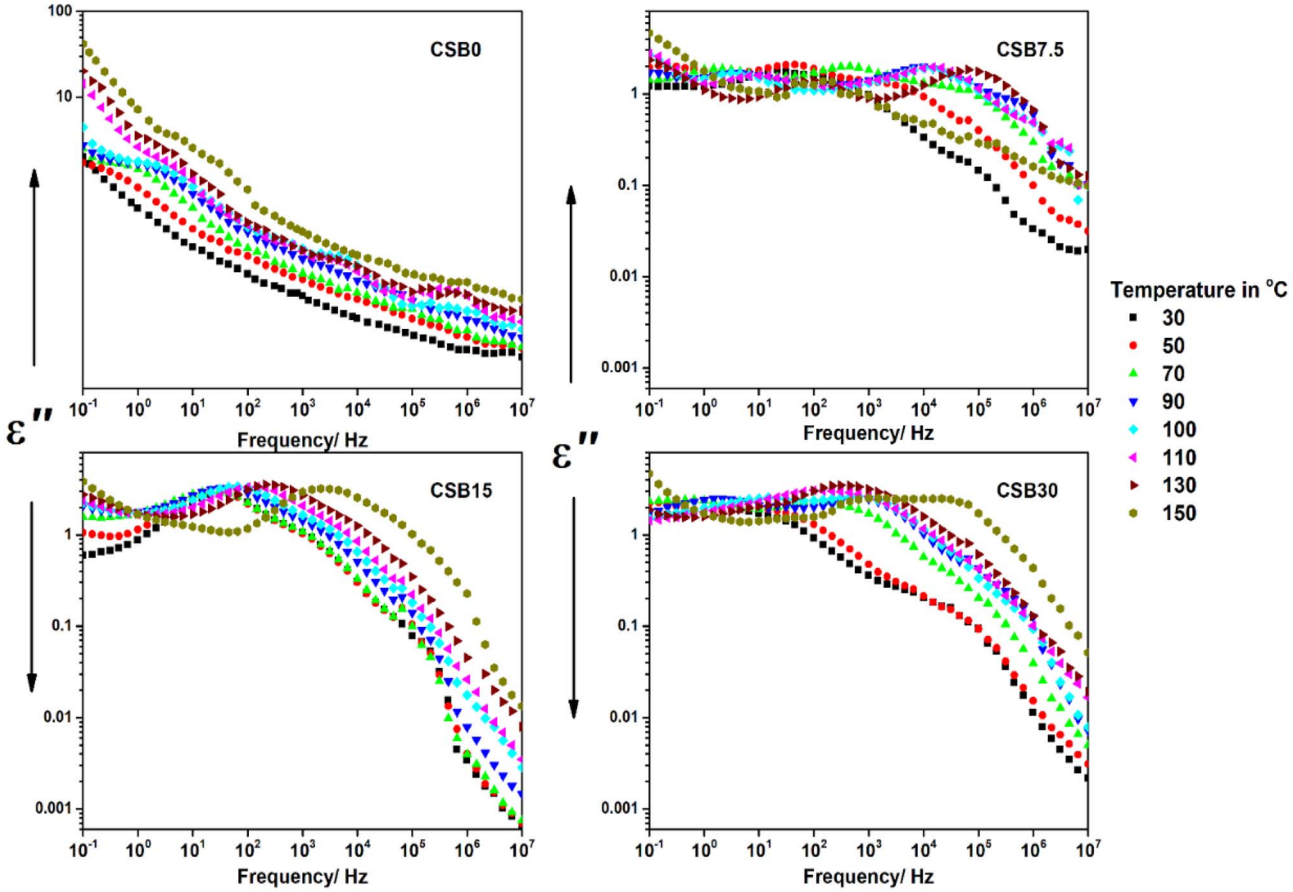

Fig. 10 Dielectric loss *vs.* frequency for the Bi_2O_3-modified SiO_2–CdO glasses at temperatures between 30 and 150 °C with a step of 20 °C as indicated.

100 kHz at 150 °C. This peak extends approximately over three decades (100 Hz–10 kHz) and broadens with the increase in temperature. As the Bi_2O_3 content increases, the mid-frequency loss moves to higher frequencies and the peak breadth grows: CSB7.5 covers roughly one decade, CSB15 covers two decades, and CSB30 covers three decades.

CSB0 shows a smooth, monotonic ε'' decay from a low frequency to a high frequency with minor peaks at a low frequency that mirrors its permittivity dispersions at low frequencies and high temperatures. CSB0's lack of a mid-frequency peak indicates that there are no Bi-induced dipolar relaxations. The steady drop indicates that loss mechanisms in CSB0 are dominated by slow space-charge or ionic contributions at a low frequency, transitioning directly into electronic/atomic polarization at a high frequency, without any distinct dipolar relaxation. In CSB7.5, the shoulder near 1 kHz comes from dipoles associated with Bi_2O_3 or non-bridging oxygens that need a moderate field rate to respond. The shift of this peak to around 100 kHz at 150 °C shows that those dipoles move faster when heated. The increase in CSB7.5's peak height as the temperature changes indicates that more dipoles engage at a higher temperature. In CSB15, the competing dynamics merge into a broader peak than noticed in CSB7.5, and the dipolar relaxation prevails. Its shift to about 4.5 kHz at 150 °C shows that Bi-related dipoles require less time to respond when heated. The wider two-decade span of the CSB15 peak reflects a broader range of Bi-site environments compared to CSB7.5. CSB30's broad peak spanning roughly 100 Hz to 10 kHz indicates the most extensive non-bridging oxygen and Bi–O network, producing multiple overlapping relaxations. The rise in CSB30's peak height shows that it has the largest dipolar polarizability of the four samples. More varied relaxation sites are produced as the content of Bi_2O_3 rises, moving mid-frequency peaks to higher frequencies and broadening them. The shift of about one decade per 120 °C rise in peak frequency for Bi-doped samples suggests an Arrhenius-type thermal activation of dipoles. At frequencies greater than 1 MHz, the same values are approached by all the samples, leaving only electronic or atomic polarization behind. CSB0's monotonic ε'' decline highlights its strong Si–O–Si network with few non-bridging oxygens for mid-frequency relaxation. Every increase in Bi_2O_3 alters the loss spectrum from smooth decay (CSB0) towards sharp, heat-shifting peaks (CSB7.5, CSB15, and CSB30). The peak breadth grows with the Bi content, reflecting a wider distribution of relaxation times linked to varied Bi or non-bridging oxygen environments.

The progressive broadening of the dielectric loss peaks and their shift to higher frequencies with the increase in Bi_2O_3

content can be directly correlated with the structural changes identified by FTIR spectroscopy and physical measurements. The coexistence of Bi–O structural environments consistent with BiO_3- and BiO_6-like units introduces dipolar sites with different local bonding symmetries and field strengths. BiO_3-type units, characterized by more asymmetric coordination, are associated with stronger local field distortions and relatively long relaxation times, contributing predominantly at lower frequencies. In contrast, BiO_6-like environments, with a higher symmetry, are associated with shorter relaxation times and contribute at higher frequencies. At low Bi_2O_3 content, these distinct local environments are sufficiently differentiated to produce separable or weakly resolved relaxation peaks, as observed for CSB7.5. With the increase in Bi_2O_3 content, the growing structural disorder and diversity of Bi-related sites lead to a broader, more continuous distribution of relaxation times, resulting in the merging of these features into a single broad loss peak spanning multiple frequency decades, as observed for CSB30. The shift of relaxation peaks to higher frequencies with both increasing temperature and Bi_2O_3 content reflects a progressive reduction in the potential barrier for dipolar hopping and reorientation. The increase in non-bridging oxygen concentration weakens the network connectivity and reduces the restoring forces acting on dipolar units, effectively lowering the depth of the local potential wells. The reduction in network rigidity lowers the energy barrier for dipolar motion, enabling faster reorientation and shifting relaxation to higher frequencies at a given temperature.

In each Bi-doped sample, the σ' shoulder or semi-peak lines up with the ε'' peak at the same frequency and temperature. For CSB7.5, the σ' feature appears around 1 kHz at 30 °C and shifts to about 10 kHz at 150 °C, and ε'' also peaks near 1 kHz at 30 °C and near 10 kHz at 150 °C. In CSB15, the σ' shoulder shows up around 500 Hz at 30 °C and moves to ~5 kHz at 150 °C, matching the ε'' peak that rises near 500 Hz at 30 °C and near 5 kHz at 150 °C. CSB30's σ' semi-peak spans ~500 Hz at 30 °C to ~10 kHz at 150 °C, and ε'' also peaks broadly in that same range under the same conditions. In contrast, CSB0 shows a smooth decrease in ε'' without a mid-frequency peak, and σ' increases steadily without exhibiting a shoulder. In other words, whenever ε'' has a clear peak in a Bi-doped glass, σ' shows a corresponding feature at the same frequency, and CSB0 lacks both.

4 Conclusion

The influence of CdO substitution by Bi_2O_3 on the physical, mechanical, and electrical properties of glasses based on the $(60 - X)$CdO–$X$$Bi_2O_3$–40$SiO_2$ mol ratio, where $X = 0.0$, 7.5, 15, and 30 mol%, was studied. Bi_2O_3 substitution depolymerizes the network, creating NBOs and increasing the free volume. A higher Bi_2O_3 content increases the permittivity and dielectric loss and makes relaxation peaks broader and move to higher frequencies with temperature. The undoped glass behaves like a rigid network with minimal dipolar or ionic contributions until temperatures exceed 130 °C. Doped glasses show mixed space-charge, dipolar, and electronic polarization mechanisms. Permittivity drops, dielectric loss peaks, and conductivity shoulders all shift to higher frequencies as the Bi_2O_3 content or temperature increases, while the onset of dispersion shifts to lower frequencies with more Bi_2O_3. The alignment of dielectric loss peaks and conductivity shoulders indicates that both loss and conduction are caused by the same mechanisms of dipolar hopping. At high frequencies above 1 MHz, all samples' permittivity and conductivity converge, showing only electronic polarization. A higher Bi_2O_3 content creates more non-bridging oxygens, which boost polarization and conductivity in these glasses. The high dielectric constant in CSB30 makes it good for energy storage capacitors, while temperature changes shift relaxation peaks for tunable operation. Dielectric loss peaks shift with the temperature from 100 to 150 °C, which makes these materials reliable for thermal monitoring sensors. These glasses offer high dielectric performance and thermal stability up to 150 °C, with potential for reprocessing, making them suitable for compact and long-lived power-electronics components used in solar inverters and wind turbine converters, while requiring responsible management of their cadmium content.

Author contributions

A. G. Darwish: data curation, methodology, formal analysis, software, writing – original draft, writing – review & editing. Mohamed I. Farouk: data curation, formal analysis, writing – original draft, writing – review & editing. Mostafa I. Abdelglil: data curation, formal analysis, writing – original draft, writing – review & editing. H. A. Abo-Mosallam: conceptualization, methodology, visualization, formal analysis, writing – original draft, writing – review & editing.

Conflicts of interest

There are no conflicts of interest to declare.

Data availability

TAll data generated or analyzed to support the findings of this study are included in this published article.

Acknowledgements

This work was supported and funded by the Deanship of Scientific Research at Imam Mohammad Ibn Saud Islamic University (IMSIU) (grant number IMSIU-DDRSP2602).

References

1 M. Ismail, *et al.*, Spectroscopic evaluation of Nd3+ doped cadmium-boro-phosphate glasses for near-IR (1060 nm) laser applications, *Opt. Mater.*, 2024, **149**, 115074.
2 M. M. Ismail, E. A. Mahdy and H. Abo-Mosallam, Spectroscopic properties of Ce3+ doped silicate glasses for near-UV white LEDs and blue laser applications, *Opt. Mater.*, 2025, **158**, 116411.
3 G. Kilic, *et al.*, First Exploration of Pr6O11 Nanoparticle Integration in Borotellurite Glasses: Synthesis,

Characterization, and Performance for Enhanced Mechanical Strength and Radiation Shielding, *Ceram. Int.*, 2025, **51**(13), 18191–18202.

4 H. Eskalen, *et al.*, Improved physical, optical, and radiation shielding characteristics of SrO-doped borate glasses: Insights from experiments and machine learning, *Ceram. Int.*, 2025, **51**(11), 14876–14891.

5 A. Shearer and J. C. Mauro, Vanadate glasses: A review of structure, properties, and applications, *J. Non-Cryst. Solids*, 2025, **657**, 123516.

6 D. Vinay, C. Devaraja and U. Deka, A comprehensive review of structural, and optical properties of boronated glasses doped with 3-d transition metal oxides (TMOs), *J. Alloys Compd.*, 2025, 180145.

7 M. Ismail Mahmoud, H. A. Abo-Mosallam and A. G. Darwish, Synthesis, mechanical, and dielectric properties of BaO–CdO–PbO–CeO2–B2O3 glass system through Sm2O3 doping for advanced dielectric applications, *Ceram. Int.*, 2025, **51**(18 part B), 25828–25836.

8 S. Athokpam, *et al.*, Electrical conductivity and dielectric study of zinc substituted tellurovanadate glass systems, *Ceram. Int.*, 2025, **51**(17), 23267–23278.

9 R. K. Mishra, *et al.*, Synergistic doping effect of La2O3 on BaO-TiO_2-SiO_2 glass-ceramics: evolution of physical, structural, morphological, and dielectric behaviour for electronics applications, *J. Alloys Compd.*, 2024, **990**, 174354.

10 I. Guizani, *et al.*, Fabrication and assessment of structural, optical and ligand field relations of silicate glass activated by ions, *Ceram. Int.*, 2025, **51**(19 part B), 29271–29282.

11 G. Sharma, *et al.*, Synthesis of biogenic calcium silicate glasses from biomass: physical, dielectric and electrical properties, *J. Non-Cryst. Solids*, 2023, **612**, 122336.

12 Y. Lu, *et al.*, Effect of silica addition on microstructure, sintering behavior, and dielectric properties of borosilicate glass/alumina composites for LTCC application, *J. Mater. Sci.: Mater. Electron.*, 2023, **34**(5), 443.

13 M. Ezzeldin, *et al.*, Impact of CdO on optical, structural, elastic, and radiation shielding parameters of CdO–PbO–ZnO–B2O3–SiO_2 glasses, *Ceram. Int.*, 2023, **49**(11), 19160–19173.

14 I. V. G. Amaya, *et al.*, Effect of CdO on the Structural and Spectroscopic Properties of Germanium–Tellurite Glass, *Materials*, 2025, **18**(8), 1739.

15 S. Y. Sorkhabi, M. Rezvani and P. R. Oskoui, Impact of MnO2 and CdO additives on optical, and physical properties of P_2O_5-ZnO-Na_2O glass for use in optical filter, *Inorg. Chem. Commun.*, 2024, **170**, 113389.

16 A. Maatouk, *et al.*, Compositional impacts of high CdO content on the structure and radiation shielding efficiency of CoO–Na_2O–B2O3 glass system, *Radiat. Phys. Chem.*, 2024, **225**, 112142.

17 K. V. Balueva, Thermophysical characterization of TeO2-WO3-Bi2O3 glasses for optical applications, *J. Non-Cryst. Solids*, 2021, **553**, 120465.

18 S. Chauhan, *et al.*, Influence of Bi_2O_3 on structural and optical characteristics of PbO B2O3 Bi_2O_3 SiO_2 glasses, *J. Non-Cryst. Solids*, 2025, **649**, 123330.

19 E. A. Mahdy, S. Ibrahim and H. Abo-Mosallam, The influence of Bi_2O_3 on structural and enhancing physical properties of Li_2O–Fe2O3–In2O3–P_2O_5 glasses, *Mater. Chem. Phys.*, 2023, **309**, 128406.

20 E. A. Mahdy, *et al.*, Dielectric and spectroscopic features of Li_2O/Fe2O3/In2O3/P_2O_5 glass systems doped with Bi_2O_3, *Appl. Phys. A*, 2025, **131**(2), 90.

21 B. Ajay Kumar, B. Sreenivas, P. Indira, A. K. Bhatnagar and P. Hima Bindu, *Opt. Mater.*, 2025, **163**, 116978.

22 T. Sumita, *et al.*, Viscosity and electrical conductivity of borosilicate glass melts with varying Na_2O content, *Mater. Lett.*, 2025, **388**, 138285.

23 B. Kalyani, *et al.*, Effect of Bi_2O_3 on AC conductivity and dielectric properties of alkali arsenate bro-bismuthate glasses, *Mater. Lett.*, 2022, **317**, 132128.

24 J. Ashok, *et al.*, Studies on dielectric dispersion, relaxation kinetics and ac conductivity of $Na_2OCuOSiO_2$ glasses mixed with Bi_2O_3-Influence of redox behavior of copper ions, *J. Alloys Compd.*, 2017, **696**, 1260–1268.

25 E. Haily, *et al.*, Structural, optical, and dielectric properties of Bi_2O_3-K_2O-TiO_2-P_2O_5 glasses and related glass-ceramics, *Phase Transitions*, 2020, **93**(10–11), 1030–1047.

26 D. Durga and N. Veeraiah, Dielectric dispersion in ZnF2-Bi_2O_3-TeO2 glass system, *J. Mater. Sci.*, 2001, **36**, 5625–5632.

27 M. Sutrisno, N. Sabri and R. Hisam, Effects of Bi_2O_3 on DC conductivity and nonlinear optical properties of mixed ionic–electronic 98 [20Li_2O-x Bi_2O_3-(80-x) TeO2]-2Ag glass system, *Appl. Phys. A*, 2021, **127**(10), 770.

28 B. Kusz, K. Trzebiatowski and R. Barczynski, Ionic conductivity of bismuth silicate and bismuth germanate glasses, *Solid State Ionics*, 2003, **159**(3–4), 293–299.

29 D. A. Aloraini and A. Saeed, Thermal neutrons-gamma rays dual-function glass shield of boron-tungsten-reinforced borosilicate glass, *Mater. Res. Bull.*, 2025, **192**, 113606.

30 D. A. Aloraini, W. Abu-raia and A. Saeed, Reinforcing silicate glass with waste lead and cadmium batteries to be used as shielding materials for gamma rays and thermal neutrons, *Sustain. Mater. Technol.*, 2025, **43**, e01257.

31 D. A. Aloraini, W. Abu-Raia and A. Saeed, An efficient attenuator for gamma rays and slow neutrons of elastic and transparent lead sodium zinc calcium borate glass, *Opt. Quant. Electron.*, 2024, **56**(3), 340.

32 N. K. Almulhem and A. Saeed, Low phonon energy Yb-oxyfluorophosphate glass doped with Er3+ or Nd3+ ions as active media for 0.991, 1.0, and 1.542 μm optical amplifiers, *Opt. Fiber Technol.*, 2025, **95**, 104454.

33 A. Makishima and J. D. Mackenzie, Direct calculation of Young's moidulus of glass, *J. Non-Cryst. Solids*, 1973, **12**(1), 35–45.

34 H. M. Zakaly, Y. S. Rammah, S. A. M. Issa, N. Almousa, A. M. El-Refaey, M. S. Shams, *et al.*, Exploring elastic mechanics and radiation shielding efficacy in neodymium (III)-enhanced zinc tellurite glasses: a theoretical and applied physics perspective, *J. Theor. Appl. Phys.*, 2023, **17**(4), DOI: 10.57647/J.JTAP.2023.1704.44.

35 N. Almousa, *et al.*, Enhancing radiation shielding transmission factors and mechanical Robustness of

borosilicate glasses through Bi_2O_3 modification: A comprehensive study, *Radiat. Phys. Chem.*, 2024, **220**, 111683.

36 A. Abd El-Moneim, *et al.*, XRD, FTIR and ultrasonic investigations of cadmium lead bismuthate glasses, *Sci. Rep.*, 2023, **13**(1), 12788.

37 A. Amat, *et al.*, Comparative spectroscopy study of TeO2–B2O3 glass system for photonic application: barium and bismuth as modifier, *Appl. Phys. A*, 2021, **127**, 1–12.

38 H. A. Thabit, *et al.*, Impact of Bi_2O_3 on the glass system B_2O_3-TeO_2–MgO–PbO on the purpose of radiation shielding efficacy, *Prog. Nucl. Energy*, 2024, **173**, 105240.

39 R. B. Jordan, *Principles of Inorganic Chemistry*, Springer International Publishing, Cham, 2024, DOI: 10.1007/978-3-031-22926-8.

40 C.-P. E. Varsamis, *et al.*, Short-range structure, the role of bismuth and property-structure correlations in bismuth borate glasses, *Phys. Chem. Chem. Phys.*, 2021, **23**(16), 10006–10020.

41 B. Topper, *et al.*, The dual role of bismuth in Li_2O–Bi_2O_3–B2O3 glasses along the orthoborate join, *J. Am. Ceram. Soc.*, 2022, **105**(12), 7302–7320.

42 N. A. Alsaif, N. Alfryyan, H. Al-Ghamdi, Y. S. Rammah, E. A. Mahdy, H. A. Abo-Mosallam, A. S. Abouhaswa, M. A. El-Sayed, *et al.*, Impact of Bi_2O_3/CdO replacement on physical, FTIR, and optical properties of high dense new CdO-BaO-Bi_2O_3-SiO_2 glass system, *Ceram. Int.*, 2025, **51**(13), 17936–17944.

43 A. Silva, *et al.*, Structure of SiO_2–MgO–Na_2O glasses by FTIR, Raman and 29Si MAS NMR, *J. Mol. Struct.*, 2011, **986**(1–3), 16–21.

44 J. Serra, *et al.*, FTIR and XPS studies of bioactive silica based glasses, *J. Non-Cryst. Solids*, 2003, **332**(1–3), 20–27.

45 A. G. Kalampounias, IR and Raman spectroscopic studies of sol–gel derived alkaline-earth silicate glasses, *Bull. Mater. Sci.*, 2011, **34**, 299–303.

46 M. El Baiomy, *et al.*, Exploring the effect of Er_2O_3 content on the structural, thermal, and physical characteristics of zinc silicate glasses, *Mater. Chem. Phys.*, 2024, **323**, 129636.

47 K. Nakamoto, *Infrared and Raman Spectra of Inorganic and Coordination Compounds*, Wiley, 2008, DOI: 10.1002/9780470405840.

48 M. L. Krishnan, M. Neethish and V. R. K. Kumar, Structural and optical studies of rare earth-free bismuth silicate glasses for white light generation, *J. Lumin.*, 2018, **201**, 442–450.

49 H. Abo-Mosallam, *et al.*, Build-up shielding-factors, and physical & mechanical properties of borosilicate glasses with varied CeO_2 contents, *RSC Adv.*, 2026, **16**(14), 12282–12294.

50 H. Abo-Mosallam, *et al.*, Design and Characterization of Eco-friendly Phospho-silicate Glasses Modified with TiO2 in the CaO-MgO-P_2O_5-SiO_2 System for Radiation Shielding Protection, *Appl. Radiat. Isot.*, 2026, 112425.

51 F. Pigeonneau, *et al.*, Physical-informed deep learning prediction of solid and fluid mechanical properties of oxide glasses, *J. Non-Cryst. Solids*, 2025, **657**, 123476.

52 S. Inaba, S. Fujino and K. Morinaga, Young's modulus and compositional parameters of oxide glasses, *J. Am. Ceram. Soc.*, 1999, **82**(12), 3501–3507.

53 A. Acikgoz, *et al.*, Structural, mechanical, radiation shielding properties and albedo parameters of alumina borate glasses: Role of CeO_2 and Er_2O_3, *Mater. Sci. Eng., B*, 2022, **276**, 115519.

54 N. A. N. Ismail, *et al.*, Enlightening the structural, elastic, and luminescence properties of transparent Zn2SiO4 glass-ceramic by precipitation of Gd2O3 as dopant, *Opt. Mater.*, 2022, **131**, 112602.

55 P. Dararutana, J. Dutchaneephet, S. Pongkrapan, N. Sirikulrat and P. Wathanakul, *Mater. Res. Innovations*, 2009, **13**, 361–363.

56 R. Bala, A . Agarwal, S. Sanghi, S. Gaur, *et al.*, The conduction mechanism and dielectric behavior of cadmium bismuth silicate glasses, *J. Phys.: Conf. Ser.*, 2023, **2603**, 012040.

57 H. A. Abo-Mosallam and S. E. Ibrahim, Impact of Ag_2O on physical and electrical properties of Li_2O-MgO-Bi_2O_3-SiO_2 glass system as promising solid state electrolytes, *Sci. Rep.*, 2025, **15**(1), 4638.